Carbon 107 (2016) 273–280

Contents lists available at ScienceDirect

Carbon

journal homepage: www.elsevier.com/locate/carbon

Determining synthesis region of the single wall carbon nanotubes in arc plasma volume

Xiuqi Fang [a, **], Alexey Shashurin [b], George Teel [a], Michael Keidar [a, *]

[a] Department of Mechanical & Aerospace Engineering, The George Washington University, Washington DC 20052, USA
[b] School of Aeronautics and Astronautics, Purdue University, West Lafayette, IN 47907, USA

ARTICLE INFO

Article history:
Received 27 April 2016
Received in revised form
22 May 2016
Accepted 26 May 2016
Available online 27 May 2016

ABSTRACT

Arc discharge is one of the most efficient and environmental friendly method to synthesize Single Wall Carbon Nanotube (SWCNT). However, due to the ultra-fast synthesis procedure, localization of the SWCNT synthesis in an arc discharge plasma volume *in situ* has been a long standing problem. This relates to the ability of controlling volumetric synthesis of nanostructures in plasmas in general. In order to better understand the mechanism of the nanotube growth in plasma, we have developed an actuator driven high-speed system that is able to extract material from the arc plasma volume during the synthesis procedure. The majority of the SWCNTs produced using arc discharge method are semiconducting with diameter of about 1.5 nm. It is shown that the growth region of SWCNTs is between 3 mm and 11 mm away from the center of the arc discharge. Dependent on the origin, the length of SWCNTs increases non-monotonically up to 500 nm, while diameter and chirality only slightly depend on the growth position.

1. Introduction

Single Walled Carbon Nanotubes (SWCNTs) were first discovered by Dr. Iijima's group using arc discharge synthesis methods in 1993 [1,2]. Since then a tremendous amount of work has been done to investigate the synthesis and applications of SWCNTs due to their outstanding electrical, mechanical and electromechanical properties [3]. SWCNTs are currently being studied for a wide range of applications such as high-capacity anode material for Lithium-ion batteries [4], paper-based ultracapacitors [5,6], sensors [7], actuators [8], solar cells [9] and bio-medical tissue enhancement [10].

Several approaches have been used to synthesize SWCNTs such as chemical vapor deposition (CVD) [11], plasma enhanced chemical vapor deposition (PECVD) [12,13], arc discharge plasma [14,15], laser ablation [16] and the electrolytic micelle distribution method [17]. Among all these methods, arc discharge plasma remains the cheapest and easiest way to obtain significant amount of SWCNTs and other 2D carbon materials [18,19]. Due to the higher growth temperature, both arc discharge plasma and laser ablation can produce SWCNTs with fewer structural defects [20,21]. However, the arc discharge process also has disadvantages over the other SWCNT production methods, in that it lacks the degree of tenability and the control over the synthesized product, and produces less pure SWCNTs as well [22]. Besides bulk production, the qualities such as uniformity of tube chirality, size distribution and ease of purification are also very important for the SWCNT products. Thus, having a comprehensive understanding of the growth mechanism for arc discharge plasma is the main challenge.

Previous simulations have been done to predict the growth region for SWCNT in arc discharge plasma with different arc currents [23]. SWCNT length dependence on the distance from the center of the arc was determined by using a continuum surface diffusion model [24]. The SWCNT producing anodic arc has been characterized by voltage-current characteristics with different gap sizes, anode compositions and background pressures [25]. The SWCNT growth region *in situ* characterization however, has not been investigated. In this paper, we describe the direct experimental localization of the nucleation and the synthesis of carbon nanotubes by *in situ* extracting the growth products from the discharge plasma. This work presents measurement of SWCNT formation region in arc discharge plasma and obtaining the relationship between the SWCNT length and the distance from the center of the

* Corresponding author.
** Corresponding author.
E-mail addresses: xiuqifang@gwmail.gwu.edu (X. Fang), keidar@gwu.edu (M. Keidar).

http://dx.doi.org/10.1016/j.carbon.2016.05.061
0008-6223/

arc. Fig. 1 shows the schematics of the electrode geometry and the tungsten probe position during the SWCNT *in situ* probing.

In order to get more precise results, probes having 50 mm lengths were exposed to the arc for 10 ms, 20 ms, 30 ms, 40 ms, 50 ms and 60 ms, separately. Those probes covered with extracted material were then characterized using a Horiba LabRam spectroscope. The SWCNT length was then measured using a SIGMA VP-02-44 SEM.

2. Experimental and simulation procedure

2.1. Experimental set-up for SWCNTs synthesis and the probing system

The SWCNT was synthesized in a stainless steel cylindrical vacuum chamber with a total volume of 4500 cm^3 (27 cm in length and 14.5 cm in diameter). A pair of electrodes, a cathode and anode, is installed along the vertical axis of the chamber. Both electrodes are made of POCO EDM-3 graphite. The cathode is a cylindrical rod with a diameter of 13 mm, while the anode is a hollow tube with inner and outer diameters of 3 mm and 5 mm, respectively. Catalysts consisted of graphite powder mixed well with nickel (300 mesh, 99.8%) and yttrium (40 mesh, 99.9) and were firmly inserted into the hollow anode. The molar ratio for the catalyst is C: Ni: Yi = 94.8: 4.2: 1.

Fig. 2 shows the schematic of the whole set-up of the plasma based SWCNT synthesis system and the actuator driven high-speed probing system. This system consists of a signal generator, DC power supply and an actuator (Ultimag Size 4 EM) which is placed 40 mm away from the center of the anode. A shutter made of steel, with a thin slit cut out, was placed between the electrodes and the probing system in order to prevent the probe from direct exposure to the arc.

Fig. 3a shows a more detailed schematic for the actuator driven high-speed probing system. A 50 mm in length, 0.5 mm in diameter tungsten wire was used as the probe to extract nanoparticles from the arc. The probe was driven by the probing system to rotate into the center of the arc. Aluminum foil was used to wrap around the shutter to prevent the probe from being exposed to the SWCNTs coming around the back of the shutter. Fig. 3b is the simulation results of the nanotube growth region following the experimental conditions (Arc current: 75 A; Distance of two electrode: 2 mm) [23]. Fig. 3c is a digital photograph of the probe probing moment.

The circuit diagram is shown in Fig. 4. The signal generator was programmable and was applied to control the probe's exposure time in the arc discharge. Before the experiment, the probe was pre-cleaned using ethanol. It has to be noted that extreme requirements to residual vacuum and probe cleaning were not applied in this work, since the SWCNTs will cover the surface of the probe.

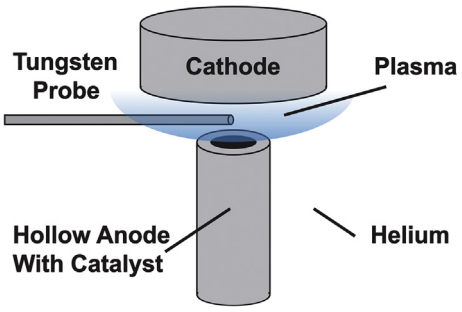

Fig. 1. Schematic presentation of the electrode geometry and the probe (tungsten probe) position during the SWCNT *in situ* probing. (A colour version of this figure can be viewed online.)

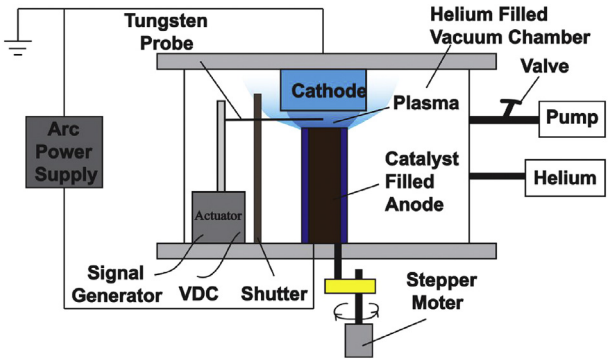

Fig. 2. Schematic of the plasma based SWCNT synthesis system with the nanotube extraction probing system. (A colour version of this figure can be viewed online.)

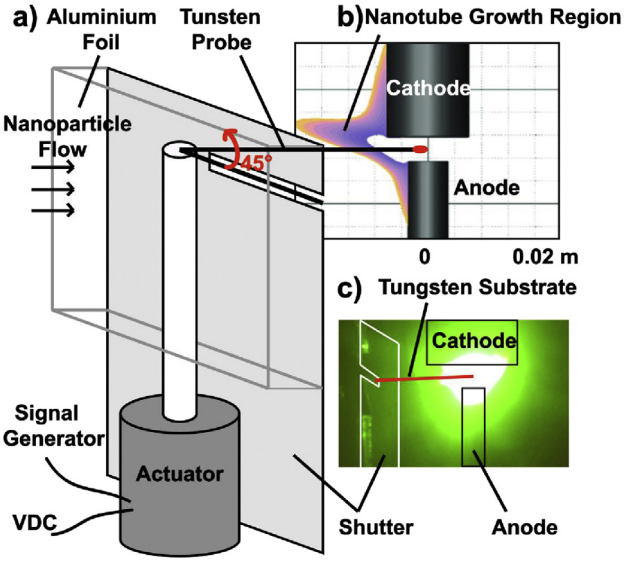

Fig. 3. **a**) Schematic of the probing system **b**) simulation result of nanotube growth region **c**) typical photograph probe extraction moment. (A colour version of this figure can be viewed online.)

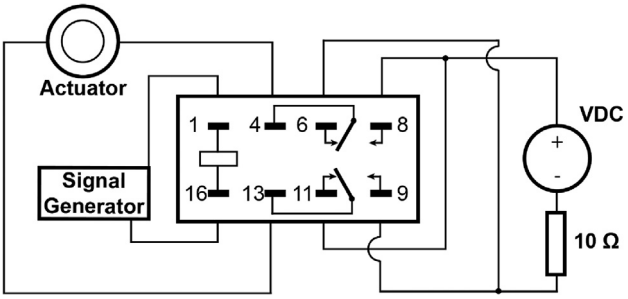

Fig. 4. Circuit diagram of the probing system.

Before the experiment, the vacuum chamber was pumped to the pressure of about 13 Pa and then high purity helium (of about 99.97%) was introduced into the chamber to about 67000 Pa. The arc electrodes were connected to an external DC power source at a fixed arc current of about 75 A. Before the experiment, the two electrodes were placed 2 mm away from each other with a thin copper wire connecting them. When the high current passes

through the whole system, the copper wire will instantaneously evaporate due to Joule heating. This exploding wire creates a medium of metallic vapor particles between the two electrodes, which allows the arc to initiate and discharge. After the arc stabilizes, the tungsten probe was then manually triggered by the signal generator and sent into the arc. With a short exposure time in the arc, the probe then returns behind the shutter with extracted nanoparticles. The probe was then roughly kept in the chamber for an additional 20 min to allow it to cool down to room temperature.

2.2. Sample analysis and characterization

All 6 samples were observed and analyzed under SEM and RAMAN Spectroscopy. Starting from the 0 mm point, 5 random SWCNTs were measured and averaged at every millimeter along each probe using the point to point feature in the SmartSEM User interface.

Fig. 5 illustrates the typical RAMAN spectrum of SWCNT (wavelength 514 nm, corresponding energy of 2.33 ev). RBM features correspond to the coherent vibration of the carbon atoms in the radial direction. The frequencies for the RBM band are very useful for identifying whether a given carbon material contains SWCNTs or not [26]. Also, the diameter of SWCNT could be determined through the equation of $\omega_{RBM} = A/d_t + B$ where $A = 234\ cm^{-1}$ and $B = 10\ cm^{-1}$ [27]. Due to the phonon wave vector confinement along the SWCNT circumferential direction and symmetry-breaking effects associated with SWCNT curvature, the G band in SWCNT is mainly composed of two peaks (G+ peak at around 1590 cm^{-1} and G-peak at around 1570 cm^{-1}). The frequency of the G band can be used for diameter characterization and to distinguish between metallic and semiconducting SWCNT [28,29]. The D band is a disorder-induced band. Both the D band and G′ band are the two strongest second-order features due to the double resonance process. As a result, they could have a much narrower spectral width than in graphite in SWCNTs ($30 - 50\ cm^{-1}$) [30]. The combination of G band intensity and G/D ratio is an effective method to evaluate the purity and defect density of SWCNTs [31]. The G* band (around 2450 cm^{-1}) can be assigned as an overtone mode of the LO phonon. The non-dispersive G* band needs to be observed as a requirement of a good sample [32].

On most of the probes, before the SWCNT starts to grow, the SEM images show granular material and the RAMAN spectrum show neither G′ peak nor RBM peak. Also in Fig. 10c at 2 mm the intensity of the G′ band is much larger than any other G′ band along the probe. Both of those instances indicate that the material along each probe is gradually transformed from other carbon material forms (most likely amorphous carbon) to SWCNTs. In addition, SEM images and RAMAN spectra show evidence that there are graphene and Multi-Walled Carbon Nanotubes (MWCNTs) which exist at certain points on the probe. Fig. 6a and b shows the RAMAN spectrum and SEM image at 3 mm on the probe with 40 ms exposure time. In the RAMAN spectrum the ratio of the G′ band and the G band is larger than two (I(G′)/I(G) > 2); also, the SEM image shows a smooth and unified surface. Both results indicate single layered graphene could be found at this area. Fig. 6c and d shows the RAMAN spectra and SEM images at 4 mm on the same probe. In Fig. 6c, a more prominent D band could be observed compared to the D band for SWCNT, and no RBM band could be observed. The more prominent D band indicates that more disorders could be found on the sample, while the lack of the RBM band is due to the outer tubes restricting the breathing mode [33]. Also, plenty of granular carbon material could be detected in Fig. 6d. All three evidences prove that MWCNTs could be found at this point.

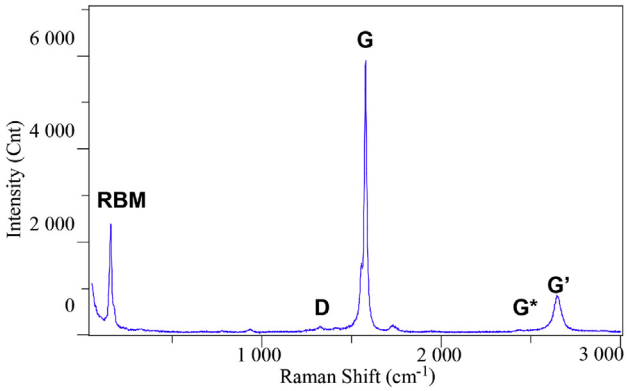

Fig. 5. The featured band for SWCNT in RAMAN spectrum.

2.3. Simulation procedure for temperature distributions

2D time-dependent numerical simulations were conducted in order to determine the temperature distribution along the tungsten probe, which was utilized in the experiment. Numerical simulations were carried out by COMSOL 5.0 software. A thermal model of the tungsten probe in the helium volume utilizes the heat transfer model. The heat transfer equation takes into account the heat conduction in the tungsten probe, heat convection from the plasma volume, and heat radiation from the probe surface:

$$\rho C_P \frac{\partial T}{\partial t} = \nabla \cdot (k \nabla T) \tag{1}$$

where ρ—tungsten density, Cp—heat capacity at constant pressure for tungsten/helium, T—temperature, and k—thermal conductivity of tungsten/helium.

The boundary conditions were formulated as follows: Temperature of one end of the tungsten wire was set to be equal to 7000 K, which is the estimated temperature in the center of the arc discharge. Heat flux (calculated by Eq. (2)) from the arc plasma in the helium atmosphere was used as a boundary condition along the tungsten probe.

$$Q_c = h \cdot (T_{ext} - T_0) \tag{2}$$

All surfaces exchanged heat with their surroundings by radiation:

$$Q_r = \varepsilon \sigma \left(T_{amb}^4 - T^4 \right) \tag{3}$$

where T_{amb}—ambient temperature, σ—Stefan-Boltzmann constant, h—heat transfer coefficient for helium, T_{ext}—external temperature, and ε—emissivity of tungsten $T_{amb} = T_{ext} = T1$ were chosen in this simulation. T1 is a variable which is related to the length of the tungsten probe, and was extracted from the results of the previous simulation [23]. The function for T1 and L could be seen in Fig. 7, and the data which was extracted from the simulation results is shown in Fig. 11.

It has to be noted that precise conditions of the heat exchange between the probe and the surroundings are unknown primarily due to the large spread of the heat transfer coefficient h, and tungsten emissivity ε. Thus, we conducted temperature simulations for the extreme range of these parameters, namely, $\varepsilon = 0.03–0.35$ and $h = 4.33–80\ W/(m^2\ K)$ [34,35]. The extreme values $e = 0.35$ and $h = 80\ W/(m^2\ K)$, provide the maximum temperature drop along the tungsten probe, and were used in the results presented below. The physical properties of tungsten utilized in the

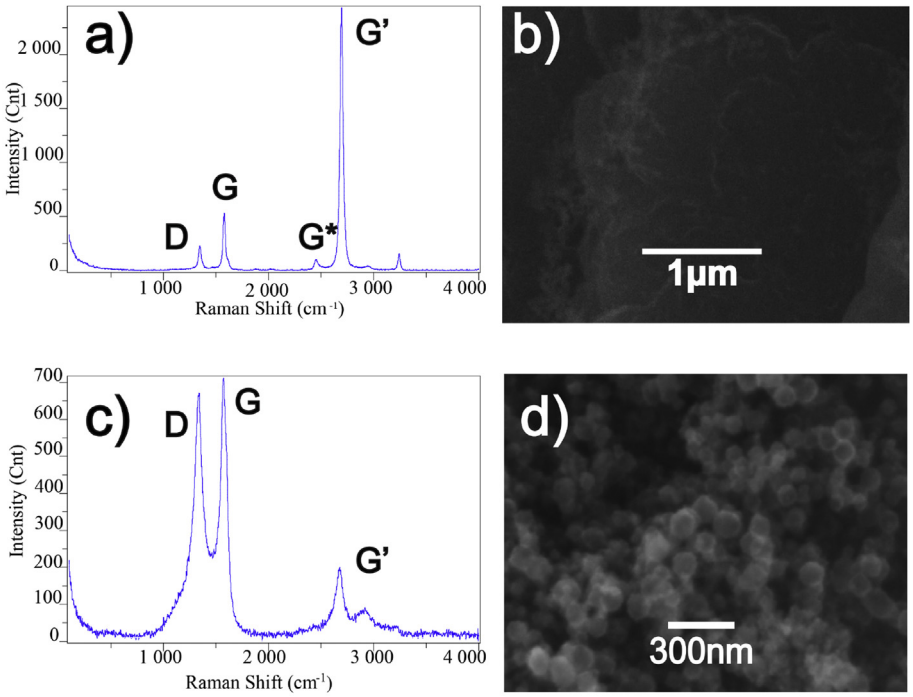

Fig. 6. **a**) RAMAN spectrum and **b**) SEM image at 3 mm on the probe with 40 ms exposure time **c**) RAMAN spectrum and **d**) SEM image at 4 mm on the same probe.

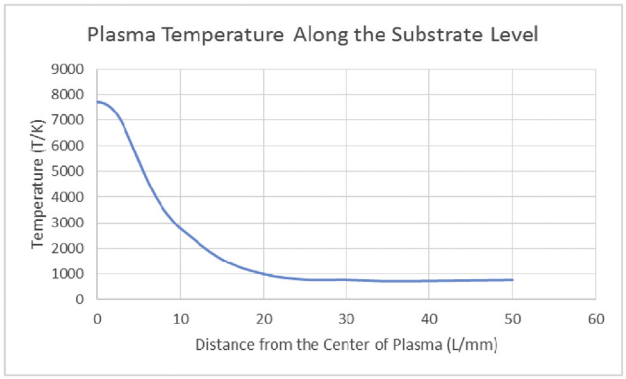

Fig. 7. Plasma temperature distribution along the probe.

simulations are summarized in Table 1.

3. Results and discussion

Fig. 8a is a drawing, which presents a typical distribution of the extracted material along the probe in the case of a 30 ms residence time. Along the probe, a black powder deposit could be seen from 3 mm to about 11 mm. Fig. 8b–d are SEM images co-related to the b (0 mm), c (5 mm), and d (10 mm) points along the probe. Point b corresponds to the edge of probe that was melted as can be seen in Fig. 8b. No carbon material could be observed at this location and the surface is relatively smooth. Point c corresponds to the darkest area along the probe. Densely packed short length SWCNTs could be found all over the probe surface (see Fig. 8c). The black coating at location d is lighter and less dense in which longer SWCNTs could be observed (see Fig. 8d). The lengths of the SWCNTs were measured using a point to point feature in the SmartSEM User interface.

Fig. 9 shows the SWCNT lengths distribution from 0 mm to 11 mm along the probes, representing the SWCNT lengths distribution along the arc plasma volume. One can see that on each probe, the lengths of SWCNTs increase from 0 nm to about 500 nm non-monotonically. Previous simulations have been done to predict the SWCNTs growth region (see Fig. 3b), and the probe measurements shown in Fig. 3 agree with the model's predictions. Moreover, probe residence time in the arc discharge does not affect the length distribution. This suggests that the probe collection is not affected by possible SWCNT drift along the arc plasma during the probe residence.

Table 1
Physical properties of tungsten utilized in simulations.

Property	Value
Thermal conductivity, k[W/(m K)]	175
Density, ρ[kg/m^3]	19,250
Heat capacity, C_P[J/(kg K)]	132
Emissivity, ε	0.35
Heat transfer coefficient, h[W/(m^2 K)]	80

Fig. 10 shows the RAMAN spectra for the considered conditions. 13 points were scanned along every probe and each scanned point was one millimeter away from each other. Four intense bands, namely, RBM (Radial Breathing Mode), D, G, G′ were observed along the spectra at around 170 cm^{-1}, 1360 cm^{-1}, 1590 cm^{-1}, and 2700 cm^{-1}.

From all the RAMAN spectra shown in Fig. 10, some general trends regarding the spectrum along each probe could be seen. One can see from Fig. 10a–c that the RBM band started to emerge at about 3 mm, while from Fig. 10d–f it can be seen that the RBM band started to come up at 5 mm. For Fig. 10a and b, both G band and D band gradually transform from wide and obtuse bands to thin and sharp peaks along the probe. Sharp G, D band at large radii on each probe indicate that SWCNTs start to appear and thus the extracted material changed from amorphous structures to SWCNTs. Typical RAMAN spectrum for several layered graphene could be found in Fig. 10c and d at 0 mm, 1 mm and 2 mm, also in Fig. 10e and f at

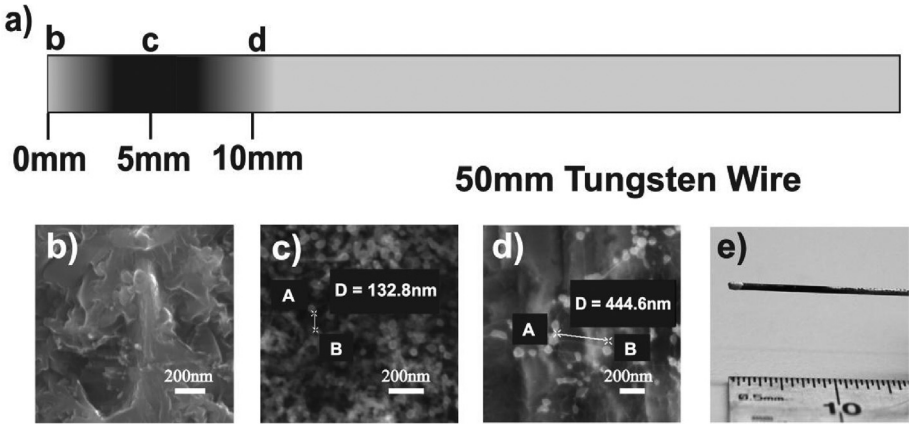

Fig. 8. A drawing **a**) and a digital image **e**) for 5 mm tungsten probe exposed to the arc for 30 ms and the SEM images of locations **b**), **c**) and **d**) that are 0 mm, 5 mm and 10 mm away from the very front of the probe, respectively.

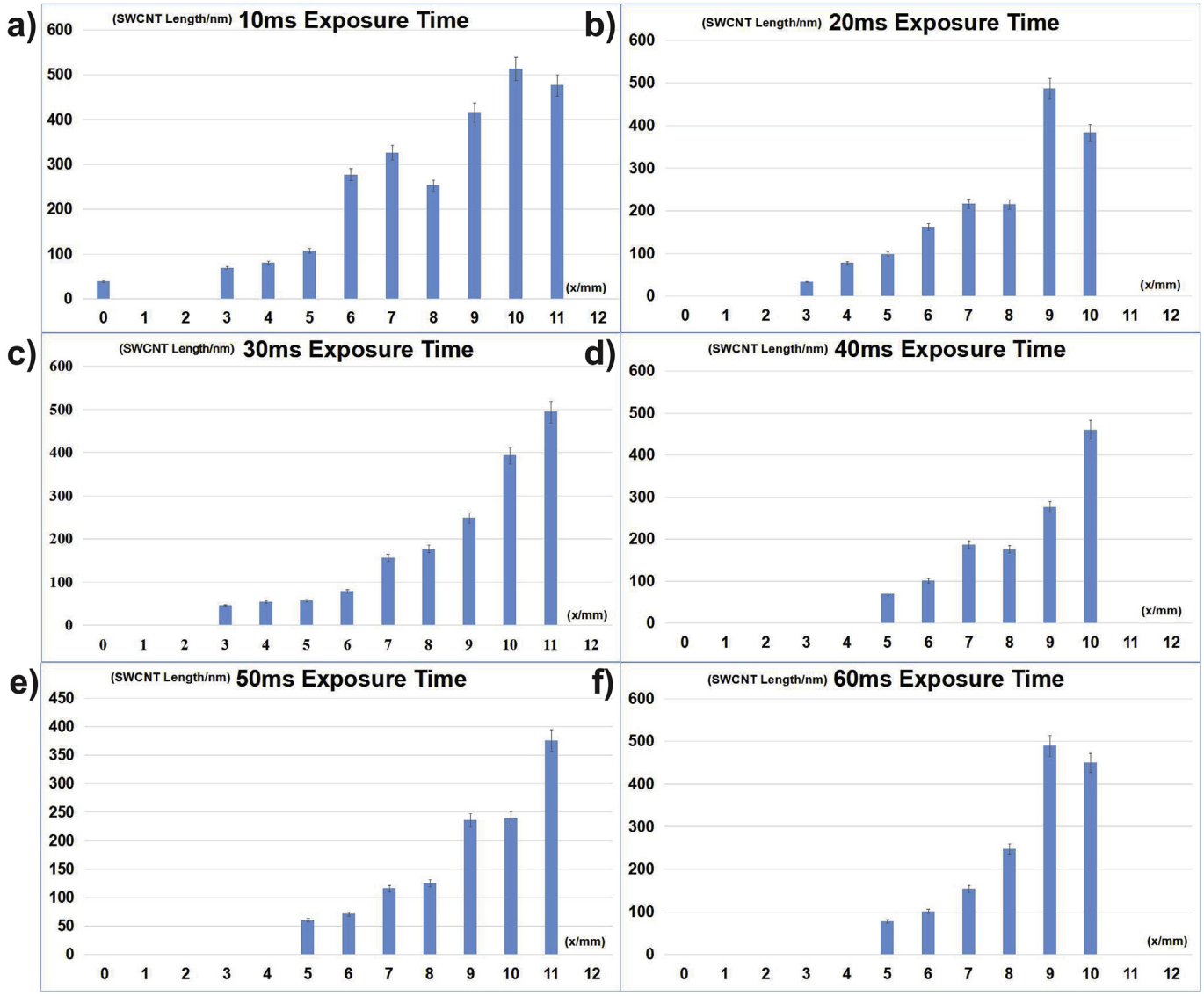

Fig. 9. SWCNT lengths distribution from the center of the arc discharge with different exposure time of **a**) 10 ms, **b**) 20 ms, **c**) 30 ms, **d**) 40 ms, **e**) 50 ms and **f**) 60 ms. (A colour version of this figure can be viewed online.)

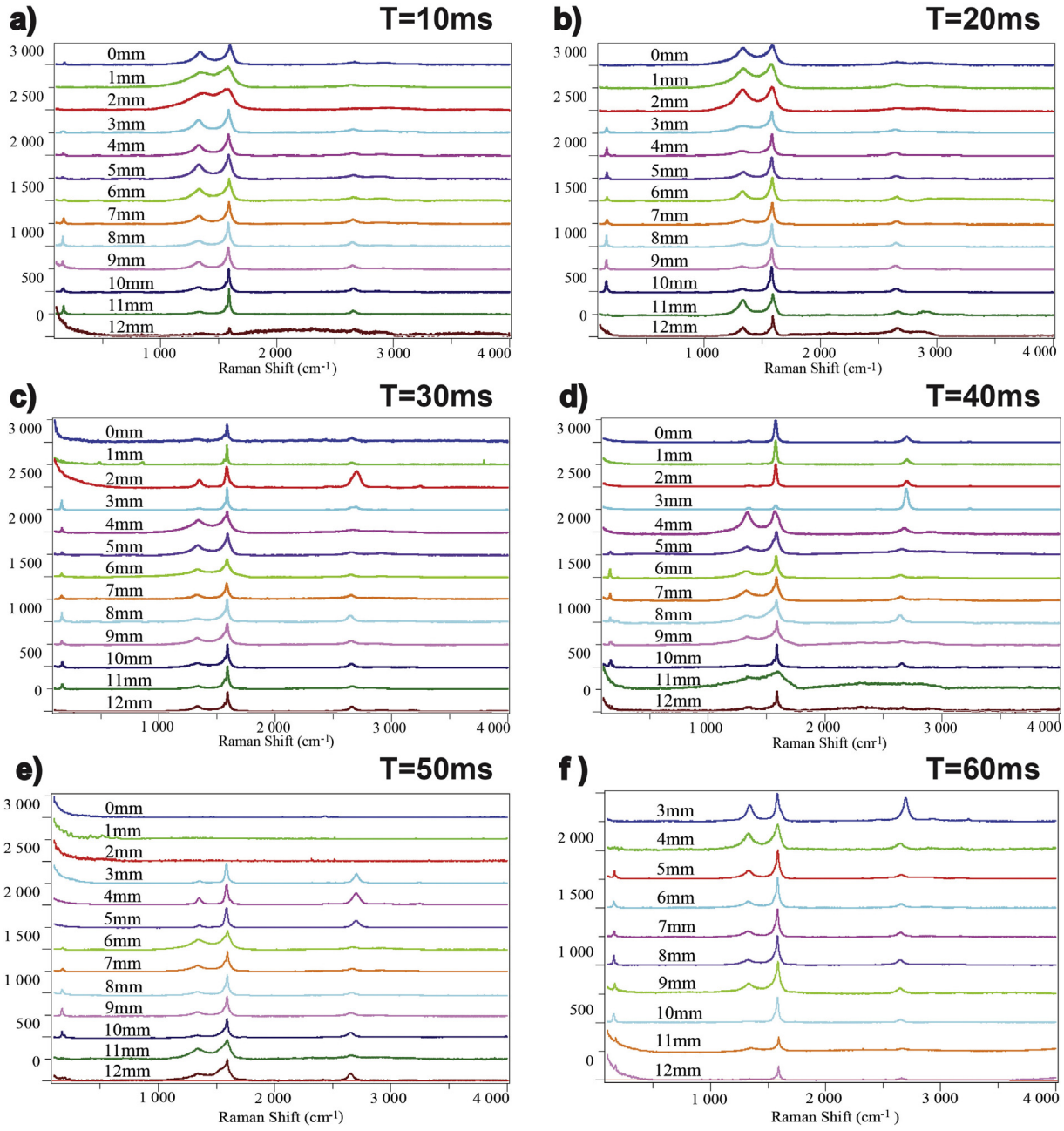

Fig. 10. SWCNT RAMAN spectra with the exposure time of **a**) 10 ms, **b**) 20 ms, **c**) 30 ms, **d**) 40 ms, **e**) 50 ms and **d**) 60 ms. Position along the probe is marked for each spectrum. (Distance is measured from the arc discharge center) (A colour version of this figure can be viewed online.)

3 mm and 4 mm. Single layered graphene spectrum appeared in Fig. 10d at 3 mm. No carbon spectrum could be observed in Fig. 10e from 0 mm to 2 mm and the sample tip melted away in Fig. 10f from 0 mm to 2 mm. This is because with longer exposure time in the arc, the probe slowly melted away due to the massive heat flux caused by the arc discharge. The whole spectrum from 4 mm to 12 mm in Fig. 10c–f majorly follow the similar trend that Fig. 10a and b have, which is that the wide and obtuse D and G bands transfer into thin and sharp peaks. This phenomenon indicates that the extracted material along each sample transferred from amorphous carbon to perfect SWCNTs. Additionally, in Fig. 10c–f, higher I(G′)/I(G) could be found at about 2–3 mm. This indicates that several layered graphene could be found around these area. It shows that when the tungsten probes reached their melting temperature with longer exposure time in the arc discharge, several layered graphene was formed around the melted area. [18,36].

Although the material attachment region on every probe is different, the RAMAN spectra at the same position after the tungsten melting point did not change as much with different exposure

Table 2
The estimated diameter of the SWCNTs with different exposure time.

Exposure time (ms)	Diameter of SWCNTs (nm)
10	1.43–1.51
20	1.49–1.57
30	1.53–1.58
40	1.55–1.58
50	1.53–1.58
60	1.56–1.60

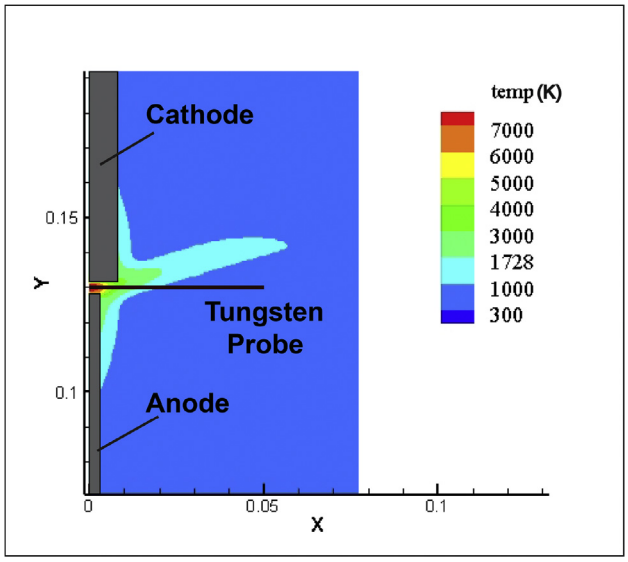

Fig. 11. Simulation of the temperature distribution inside the arc chamber. 8 s from the arc initiation. (A colour version of this figure can be viewed online.)

times. This indicates that the extracted material on the tungsten probes is formed at that position in the arc instead of being formed at different positions and transferred by the heat flux to the probe.

Table 2 shows the calculated range of diameters of the SWCNTs with different exposure times to the arc discharge plasma. Previous experiment shows that the produced nanotube is a mixture of metallic and semiconductor SWCNTs (mostly semiconductor SWCNTs) [22]. The fact that SWCNTs of a stable diameter have been produced regardless of the exposure time indicates that the diameters for SWCNTs have been defined before they start growing, and the diameters were kept during the growth.

It is known that the SWCNT growth in arc discharge plasma is strongly affected by the catalyst particles [21]. During the SWCNT synthesis process the temperature in the center of the plasma is extremely high (about 5000 K). To illustrate this point we have performed a numerical simulation of arc discharge using previously developed code [24]. Fig. 11 shows typical simulated temperature distribution inside the arc chamber. During the probe's residence in the arc, heat transfer from the arc plasma to the probe leads to an increase in probe temperature. This is apparent from the fact that the probe's edge is melted if the probe residence time exceeds 30 ms. When the surface of the tungsten wire is higher than or equal to the melting temperature of Ni (1728 K), there is a possibility that molten nickel nanoparticles will be present along the probe surface allowing SWCNT to grow at the probe surface. This effect might interfere with collected data interpretation that SWCNT distribution along the probe mirrors SWCNT distribution in the plasma volume.

In order to estimate such possibilities, we have performed time dependent numerical simulation of the probe temperature in the presence of hot arc plasma using plasma simulation code and COMSOL package. Fig. 12 shows the results of 2D simulation of the temperature distribution (the temperature ranges from 7000 K to 450 K) along the surface of the probe with the residence time of about 30 ms. One can see that 2.51 mm away from the melting point of the probe, the surface of the tungsten wire has dropped below 1728 K. Table 3 provides the position on the tungsten probe which reaches surface temperature of 1728 K as a function of the probe residence time.

This result indicates that along most parts of the probe, nickel nanoparticles collected from the arc plasma are likely solidified and thus cannot promote SWCNT growth at the probe's surface. This suggests that SWCNTs collected by the probe have originated from the arc plasma volume, and that the distribution of SWCNTs along

Table 3
Position when the tungsten probe surface temperature reaches the 1728 K with different exposure time to the arc discharge.

Exposure time in the arc (t/ms)	Position on the tungsten probe when temperature reach 1728 K (d/mm)
10	1.39
20	2.02
30	2.51
40	2.92
50	3.29
60	3.62

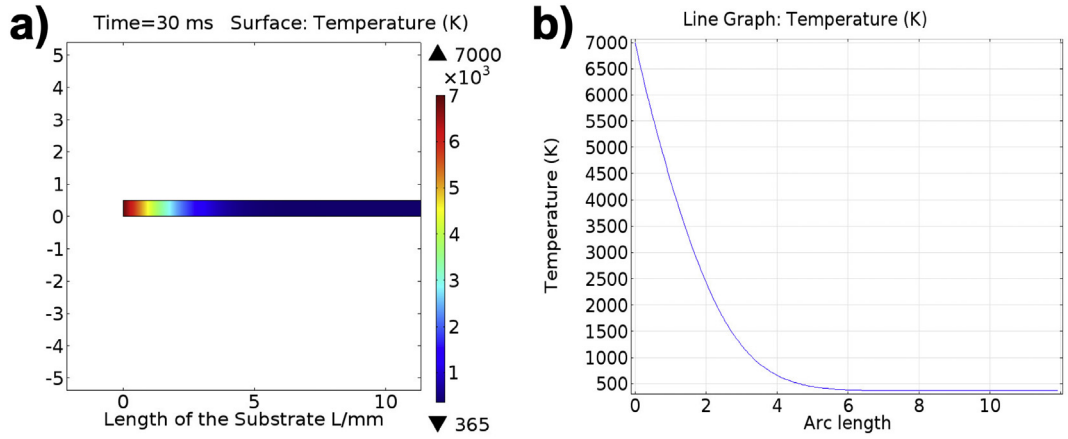

Fig. 12. **a**) Simulation results for 2D temperature distribution on the Tungsten probe with 30 ms exposure to the arc **b**) Temperature distribution along the centerline of the tungsten probe. (A colour version of this figure can be viewed online.)

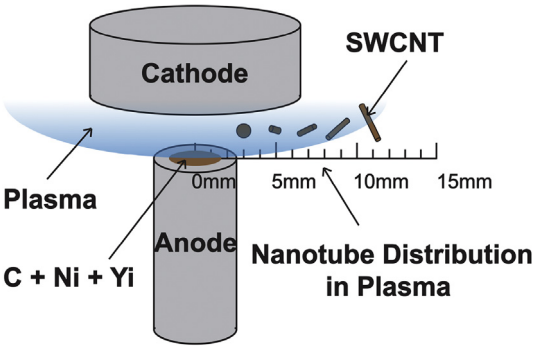

Fig. 13. Trend showing SWCNT growth in an arc plasma.

the probe surface are a good representation of SWCNT distribution along the plasma volume.

Hence, based on the probe surface analysis we have determined that the growth region for SWCNTs in arc plasma is within 3 mm–11 mm away from the center of the arc discharge. It should be pointed out that SWCNT length increases with distance from the arc core, which is in agreement with previous model predictions [21]. Schematically the trend showing SWCNT growth is illustrated in Fig. 13.

4. Conclusion

The location of SWCNTs synthesized in an arc discharge plasma has been successfully determined by an actuator driven high-speed probing system. We have determined that the SWCNT growth region, in the case of arc plasma synthesis, is between 3 mm and 11 mm away from the center of the arc discharge. Dependent on the origin of nucleation, the length of SWCNT increases non-monotonically up to 500 nm while diameter and chirality only slightly depend on the growth position.

Acknowledgment

The authors benefited from fruitful discussions with Dr. Y. Raitses and Dr. M. Shneider. The authors thank Dr. M. Kundrapu for help with numerical simulations of arc discharge. This work was supported the U.S. Department of Energy, Office of Science, Basic Energy Science, Materials Sciences and Engineering Division.

References

[1] S. Iijima, T. Ichihashi, Single-shell carbon nanotubes of 1-nm diameter, Nature 363 (1993) 603–605.
[2] D. Bethune, C. Klang, M. De Vries, G. Gorman, R. Savoy, J. Vazquez, et al., Cobalt-catalysed growth of carbon nanotubes with single-atomic-layer walls, Nature 363 (1993) 605–607.
[3] Z. Spitalsky, D. Tasis, K. Papagelis, C. Galiotis, Carbon nanotube–polymer composites: chemistry, processing, mechanical and electrical properties, Prog. Polym. Sci. 35 (2010) 357–401.
[4] H.X. Zhang, C. Feng, Y.C. Zhai, K.L. Jiang, Q.Q. Li, S.S. Fan, Cross, stacked carbon nanotube sheets uniformly loaded with SnO2 nanoparticles: a novel binder free and high capacity anode material for Lithium ion batteries, Adv. Mater. 21 (2009) 2299–2304.
[5] J. Li, X. Cheng, J. Sun, C. Brand, A. Shashurin, M. Reeves, et al., Paper-based ultracapacitors with carbon nanotubes-graphene composites, J. Appl. Phys. 115 (2014) 164301/1–164301/5.
[6] J. Li, X. Cheng, A. Shashurin, M. Keidar, Review of electrochemical capacitors based on carbon nanotubes and graphene, Graphene 1 (2012) 1–13.
[7] J. Kong, N.R. Franklin, C. Zhou, M.G. Chapline, S. Peng, K. Cho, et al., Nanotube molecular wires as chemical sensors, Science 287 (2000) 622–625.
[8] R.H. Baughman, C. Cui, A.A. Zakhidov, Z. Iqbal, J.N. Barisci, G.M. Spinks, et al., Carbon nanotube actuators, Science 284 (1999) 1340–1344.
[9] A. Kongkanand, R. Martínez Domínguez, P.V. Kamat, Single wall carbon nanotube scaffolds for photoelectrochemical solar cells. Capture and transport of photogenerated electrons, Nano Lett. 7 (2007) 676–680.
[10] B. Holmes, X. Fang, A. Zarate, M. Keidar, L.G. Zhang, Enhanced human bone marrow mesenchymal stem cell chondrogenic differentiation in electrospun constructs with carbon nanomaterials, Carbon 97 (2016) 1–13.
[11] A.M. Cassell, J.A. Raymakers, J. Kong, H. Dai, Large scale CVD synthesis of single-walled carbon nanotubes, J. Phys. Chem. B 103 (1999) 6484–6492.
[12] M. Meyyappan, L. Delzeit, A. Cassell, D. Hash, Carbon nanotube growth by PECVD: a review, Plasma Sour. Sci. Technol. 12 (2003) 205–216.
[13] I. Levchenko, A.E. Rider, K. Ostrikov, Deterministic shape control in plasma-aided nanotip assembly, Appl. Phys. Lett. 90 (19) (2007) 193110.
[14] M. Keidar, I. Levchenko, T. Arbel, M. Alexander, A.M. Waas, K.K. Ostrikov, Increasing the length of single-wall carbon nanotubes in a magnetically enhanced arc discharge, Appl. Phys. Lett. 92 (2008), 043129/1-043129/3.
[15] M. Keidar, I. Levchenko, T. Arbel, M. Alexander, A.M. Waas, Kostya (Ken) Ostrikov, Magnetic field-enhanced synthesis of single wall carbon nanotubes in arc discharge, J. Appl. Phys. 103 (2008), 094318.
[16] Z. Liu, D. Zhang, S. Han, C. Li, T. Tang, W. Jin, et al., Laser ablation synthesis and electron transport studies of tin oxide nanowires, Adv. Mater. 15 (2003) 1754–1757.
[17] G. Cao, D. Liu, Template-based synthesis of nanorod, nanowire, and nanotube arrays, Adv. Colloid Interface Sci. 136 (2008) 45–64.
[18] Growth of carbon nanostructures by arc discharge and laser ablation, in: M. Meyyappan (Ed.), Carbon Nanotubes: Science and Applications, CRC press, 2004, pp. 65–66.
[19] A. Shashurin, M. Keidar, Synthesis of 2D materials in arc plasmas, J. Phys. D Appl. Phys. 48 (2015) 314007/1–314007/9.
20 M. Keidar, I. Beilis, Modeling of atmospheric-pressure anodic carbon arc producing carbon nanotubes, Journal of Applied Physics 106 (2009) 103304/1–103304/6.
[21] M. Keidar, Factors affecting synthesis of single wall carbon nanotubes in arc discharge, J. Phys. D Appl. Phys. 40 (2007) 2388–2393.
[22] O. Volotskova, J.A. Fagan, J.Y. Huh, F.R. Phelan Jr., A. Shashurin, M. Keidar, Tailored distribution of single-wall carbon nanotubes from arc plasma synthesis using magnetic fields, ACS Nano 4 (2010) 5187–5192.
[23] M. Kundrapu, M. Keidar, Numerical simulation of carbon arc discharge for nanoparticle synthesis, Phys. Plasmas (1994-present) 19 (2012), 073510/1-073510/9.
[24] M. Kundrapu, J. Li, A. Shashurin, M. Keidar, A model of carbon nanotube synthesis in arc discharge plasmas, J. Phys. D Appl. Phys. 45 (2012) 315305/1–315305/11.
[25] A. Shashurin, M. Keidar, I. Beilis, Voltage-current characteristics of an anodic arc producing carbon nanotubes, J. Appl. Phys. 104 (2008) 63311/1–63311/5.
[26] M.S. Dresselhaus, G. Dresselhaus, R. Saito, A. Jorio, Raman spectroscopy of carbon nanotubes, Phys. Rep. 409 (2005) 47–99.
[27] M. Milnera, J. Kürti, M. Hulman, H. Kuzmany, Periodic resonance excitation and intertube interaction from quasicontinuous distributed helicities in single-wall carbon nanotubes, Phys. Rev. Lett. 84 (2000) 1324–1327.
[28] A. Jorio, M. Pimenta, A. Souza Filho, R. Saito, G. Dresselhaus, M. Dresselhaus, Characterizing carbon nanotube samples with resonance Raman scattering, New J. Phys. 5 (2003) 139/1–139/17.
[29] M. Dresselhaus, G. Dresselhaus, A. Jorio, A.G. Souza Filho, G.G. Samsonidze, R. Saito, Science and applications of single-nanotube Raman spectroscopy, J. Nanosci. Nanotechnol. 3 (2003) 19–37.
[30] A. Jorio, C. Fantini, M. Dantas, M. Pimenta, A. Souza Filho, G.G. Samsonidze, et al., Linewidth of the Raman features of individual single-wall carbon nanotubes, Phys. Rev. B 66 (2002) 115411/1–115411/8.
[31] Y. Miyata, K. Mizuno, H. Kataura, Purity and defect characterization of single-wall carbon nanotubes using Raman spectroscopy, J. Nanomater. 2011 (2011) 18/1–18/7.
[32] A.C. Ferrari, D.M. Basko, Raman spectroscopy as a versatile tool for studying the properties of graphene, Nat. Nanotechnol. 8 (2013) 235–246.
[33] J. Hodkiewicz, Characterizing carbon materials with Raman spectroscopy, Thermo Sci. Appl. Note (2010) 51901.
[34] Y.S. Touloukian, D.P. DeWitt, Thermophysical Properties of Matter-the TPRC Data Series, in: Thermal Radiative Properties-metallic Elements and Alloys. (Reannouncement). Data Book, vol. 7, Purdue Univ., Lafayette, IN (United States), 1970, pp. 776–777. Thermophysical and Electronic Properties Information Center.
[35] J.H. Lienhard, A heat transfer textbook, Cour. Corp. (2013) 21.
[36] X. Fang, A. Shashurin, M. Keidar, Role of substrate temperature at graphene synthesis in an arc discharge, J. Appl. Phys. 118 (2015) 103304/1–103304/6.